Electronic Supporting Information for

Distinguishing Between Bulk and Edge Hydroxyl Vibrational Properties of 2:1 Phyllosilicates via Deuteration

Jacob A. Harvey,[a] Cliff T. Johnston,[b] Louise J. Criscenti,[a] Jeffery A. Greathouse[a]

[a] Geochemistry Department, Sandia National Laboratories, Albuquerque, New Mexico 87125, United States

[b] Crop, Soil and Environmental Sciences, Purdue University, West Lafayette, Indiana 47907, United States

Table of Contents

1. Methods

1.1 Computational Methods

1.1.1 DFT Methods

The orthogonal crystal structure for pyrophyllite was used as a starting point for all systems.[1] As discussed in previous works[2] there exists two possible conventions for the orientation of the orthogonal pyrophyllite unit cell; pyrophyllite-like and montmorillonite-like. In this work we have chosen the montmorillonite-like orientation. The 010 and 110 crystallographic faces were explored. Both faces have multiple possible "cuts" to create an edge however the "A" cut from Pakkanen et al.[3] has been shown to have the smallest free energy of cleavage and are the focus of the work here. Figure 1 in the Manuscript depicts the unit cell of pyrophyllite with the indicated cuts.

The crystal structure was optimized using the projector-augmented wave approach[4] implemented in the Vienna Ab Initio Simulation Package (VASP v5.3).[5] The Perdew-Burke-Ernzerhof revised for solids (PBESol) exchange correlation functional[6] was used in conjunction with van der Waals corrections applied via the DFT-D3 method with Becke-Jonson damping.[7] All calculations were performed at the Γ point. A three-step procedure was used for geometry optimizations; (1) ions optimized, (2) cell optimized with constant shape, and (3) ions reoptimized. A 400 eV cutoff was used for the planewave basis set during ion optimizations while a 520 eV cutoff was using during cell optimizations. Optimizations proceeded until all forces were less than .03 $eV \cdot Å^{-1}$. Calculated cell parameters are given in Table S1. Using a single unit cell, edges were created on the 010 and 110 face as described above and a 15 Å vacuum gap was placed in the direction perpendicular to the cut to minimize interactions between periodic images of edges. Hydroxyl groups were added to undercoordinated Si atoms, while hydrogens were added to undercoordinated O atoms to form the final edge structures depicted in Figure 1 in the Manuscript. Deuterated structures were created by changing the mass parameter of the edge H atoms to 2.018 amu.

Table S1. Experimental and computationally determined lattice parameters for pyrophyllite.

	a (Å)	b (Å)	c (Å)	α (°)	β (°)	γ (°)
Lee and Guggenheim (experimental)[8]	5.160	8.966	9.347	91.18	100.46	89.64
Drits et al.[1]	5.185	8.923	9.347	90.00	90.00	90.00
Kremleva et al.[2]	5.220	9.070	9.850	91.10	100.00	89.70
Churakov[9]	5.219	9.033	12.000	90.00	90.00	90.00
This work	5.177	8.909	9.332	90.00	90.00	90.00

Vibrational frequencies were calculated within VASP using the density functional perturbation theory formalism (DFPT).[10] Intensities in this manner are calculated as:

$$I(\omega) = \sum_{\alpha=1}^{3} \left| \sum_{s=1}^{M} \sum_{\beta=1}^{3} Z^{*}_{\alpha\beta}(s) e_{\beta}(s) \right|^2 \quad (1)$$

where α, β are Cartesian polarizations, $Z^{*}_{\alpha\beta}(s)$ is the Born effective charge of atom 's', and $e_{\beta}(s)$ is the vibrational eigenvector of ω^{th} mode. A lorentzian function was calculated for each frequency to simulate broadening effects and the total spectrum formed by summing all calculated lorentzians. Assignment of frequencies to specific modes was done by visualizing each normal mode in J-ICE.[11]

1.1.2 Classical MD Methods

1.1.2.1 System

The bulk pyrophyllite system was created by producing a 6x4x4 supercell using the optimized unit cell described above. Edge structures began by repeating the unit cell four times in the direction perpendicular to the desired edge. This ensures a > 30 Å distance between edges and limits the interaction between the two. The cut depicted in Figure 1 of the Manuscript was made on the 010 and 110 faces. At this point, hydrogens were added to fill the coordination of oxygens and hydroxyl groups were added to fill the coordination of silica atoms. Aluminum atoms were left as five coordinate with a single hydroxyl group. A vacuum of region of ~20 Å was then placed at the created edge to prevent the interaction of periodic images. This cut surface was then

repeated 6 times in the direction parallel to the cut to create a 1D layer and then each layer was repeated to create four stacked 1D sheets. The final structure for both crystallographic faces contains 3984 atoms and is depicted in Figure 1 of the Manuscript. Deuterated structures were created by changing the mass of the edge hydrogens to 2.018 amu. All other force field parameters remained the same and are described below.

1.1.2.2 Simulation Parameters

Classical molecular dynamics simulations were run using the Large-scale Atomic/Molecular Massively Parallel Simulator (LAMMPS) package.[12] The ClayFF force field was used for all simulations.[13] Recently developed metal-hydroxyl angle bending terms were included for the edge structures and also applied to internal Al-O-H groups.[14] All simulation parameters are included in Table S2-S4. Short range interactions were cut at 10 Å while an Ewald summation was used for long-range Coulombic interactions with an accuracy of .0001 units.[15] The rRESPA multi-timescale integrator was used with two loops where short-range interactions were computed every .5 fs while all other interactions were computed every 1 fs.[16]

Table S2. Atomic charges and Lennard Jones parameters for all pyrophyllite atoms.

Atom	q	σ (Å)	ε (kcal · mol^{-1})
Al	1.575	4.271	1.330e-6
H	.425	0.000	0.000
O (internal)	-1.050	3.166	.155
O (edge)	-0.950	3.166	.155
Si	2.100	3.302	1.840e-6

Table S3. Bond force field parameters (Morse: $E = D[1 - e^{-\alpha(r - r_o)}]^2$)

Bond Type	D (kcal · mol^{-1})	α (Å^{-1})	r_o (Å)
O-H (internal/edge)	132.2491	2.1815	0.945

Table S4. Angle force field parameter (Harmonic: $E = k(r - r_o)^2$)

Angle Type	k (kcal · mol^{-1})	θ_o (degrees)
Si-O-H	15.000	100.00
Al-O-H (internal/edge)	15.000	110.00

Simulations for bulk and edge structures were performed using the following general simulation procedure. Initial velocities were created using the Maxwell-Boltzmann distribution for the target temperature of 298 K. A 1 ns run was performed at 298 K with velocity rescaling, followed by an additional 1 ns of NVE simulation without velocity rescaling. At this point the pressure in the system was found to be quite high (> 20000 atm, Figure S1). In order to relax the pressure a 1 ps anisotropic NPT simulation was performed with a starting pressure of 10000 atm and final pressure of 1 atm. During this simulation a small timestep of .001 fs was used, resulting in 1000000 MD steps. The timestep was then ramped back up to the desired value of 1 fs by running 1000000 NPT MD steps at .01 and .1 fs timesteps. A final NPT run was conducted for 10 ns with a 1 fs timestep at 1 atm. All NPT runs were performed using the Berendsen thermostat/barostat.[17] The applied thermostat/barostat was then turned off for a 10 ns NVE run, and a final NVE "production" stage was run for 5 ns. The simulation length was tested by calculating the IR spectrum for bulk pyrophyllite for 1, 5, and 10 ns simulations (Figure S2); and the IR spectrum for 110 protonated pyrophyllite edge for 5, and 10 ns simulations (Figure S3). Little improvement was seen when going from 5 ns to 10 ns and therefore 5 ns provided sufficient accuracy for the study presented here. Snapshots were saved every 2 fs during production runs. Error bars were calculated using block averaging and are presented for the 95% confidence interval.[18]

1.1.2.3 Classical Infrared Spectrum

The infrared lineshape from classical MD simulations was calculated via the Fourier transform of the total dipole moment time-correlation function (TCF)[19]:

$$I(\omega) = \frac{1}{2\pi}\int_{-\infty}^{\infty} dt e^{-i\omega t}\langle \delta\vec{M}(0)\cdot\delta\vec{M}(t)\rangle \quad (2)$$

where $\vec{M}(t) = \sum_{i=1}^{N} q_i \vec{r}_i(t)$ is the total dipole moment TCF with q_i and $\vec{r}_i(t)$ being the charge and position of atom i at time t. Given periodic boundary conditions, the positions of atoms are often discontinuous therefore the mathematically equivalent form[20] was used here:

$$I(\omega) = \frac{1}{2\pi\omega^2}\int_{-\infty}^{\infty} dt e^{-i\omega t}\left\langle \frac{d\vec{M}(0)}{dt} \cdot \frac{d\vec{M}(t)}{dt} \right\rangle$$
$$= \frac{1}{2\pi\omega^2}\int_{-\infty}^{\infty} dt e^{-i\omega t}\left\langle \left(\sum_{i=1}^{N} q_i \vec{v}_i(0)\right) \cdot \left(\sum_{i=1}^{N} q_i \vec{v}_i(t)\right) \right\rangle \quad (3)$$

where $\vec{v}_i(t)$ is the velocity of atom i at time t. The TCF represented in equation 3 is known as the electrical flux-flux correlation function. We note that this charge-weighted version of the widely used power spectrum (ie. Fourier transform of the velocity autocorrelation function) results in a significantly improved spectrum for bulk pyrophyllite (Figure S4). This is particularly true in the bending region of the spectrum where only one peak is observed in the power spectrum while three peaks are observed in the flux-flux time correlation function version, which more closely matches the experimental spectrum (Figure 2 in Manuscript). It was found that taking the Fourier transform of the entire TCF resulted in negative intensities. These can be removed by squaring the results infrared spectrum[21] and then smoothed using a running average. However, this effectively changes the ratio of peak heights. Instead, the TCF was cut at the point in which it decays to 0; which typically occurred within 10 ps. The Fourier transform was then taken on this smaller portion which resulted in a smooth IR lineshape with no negative intensities. The calculated IR lineshape for bulk pyrophyllite taken from cutting the TCF at various time points is shown in Figure S5. Cutting the TCF too early (5 ps) reduces the resolution of the spectrum, while cutting it too long (20 ps) increases the noise. In this context, 10 ps was found to provide the optimal balance between resolution and noise and was used throughout this study. Due to the short time duration between frames (2 fs), the TCF would be calculated from highly correlated snapshots. In an attempt to remove this correlation, various waiting times between new time zeroes in the TCF calculation were tested (Figure S6). A waiting time of 20 fs between time zeroes appears to provide reasonably small error bars while also removing some of the correlation between snapshots and was therefore used in all calculations presented here unless otherwise noted.

1.2 Experimental Methods

The pyrophyllite sample was obtained from the American Petroleum Institute Clay Mineral Standards Project No. 49 from Robbins, North Carolina .[22] The sample was lightly ground in an agate mortar and pestle and 15 mg of the samples dispersed in 1.5 mL of distilled-deionized H_2O. One mL of this aqueous pyrophyllite suspension was placed in the trough of a 9-bounce horizontal trough ATR cell from Pike Scientific with a ZnSe internal reflection element (Pike Technologies, Madison, WI). Reference spectra of liquid H_2O, D_2O were obtained prior to pyrophyllite analysis. The aqueous suspension in the ATR cell was allowed to dry resulting in a uniform deposit of pyrophyllite. The samples were 'washed' ten times by adding one mL of distilled-deionized H_2O and gently shaking the cell to remove any excess pyrophyllite. The ATR-FTIR spectrum of the resulting 'washed' deposit was compared to the initial deposit revealing that a stable deposit was obtained. One mL of liquid D_2O was added to the cell and the cell was sealed to prevent exposure of H_2O vapor and allowed to equilibrate for 6 hours. The cell was then connected to a source of dry N_2 (H_2O-free) and the spectra were obtained as a function of time as the sample was allowed to dry in the presence of D_2O. The FTIR measurements were performed with a Nicolet 6700 FTIR (Thermo Scientific) using a liquid nitrogen cooled MCT detector. The scans were obtained in the range from 4000 to 700 cm^{-1} with a resolution of 4 cm^{-1}, and 64 scans per sample.

2. Additional Figures

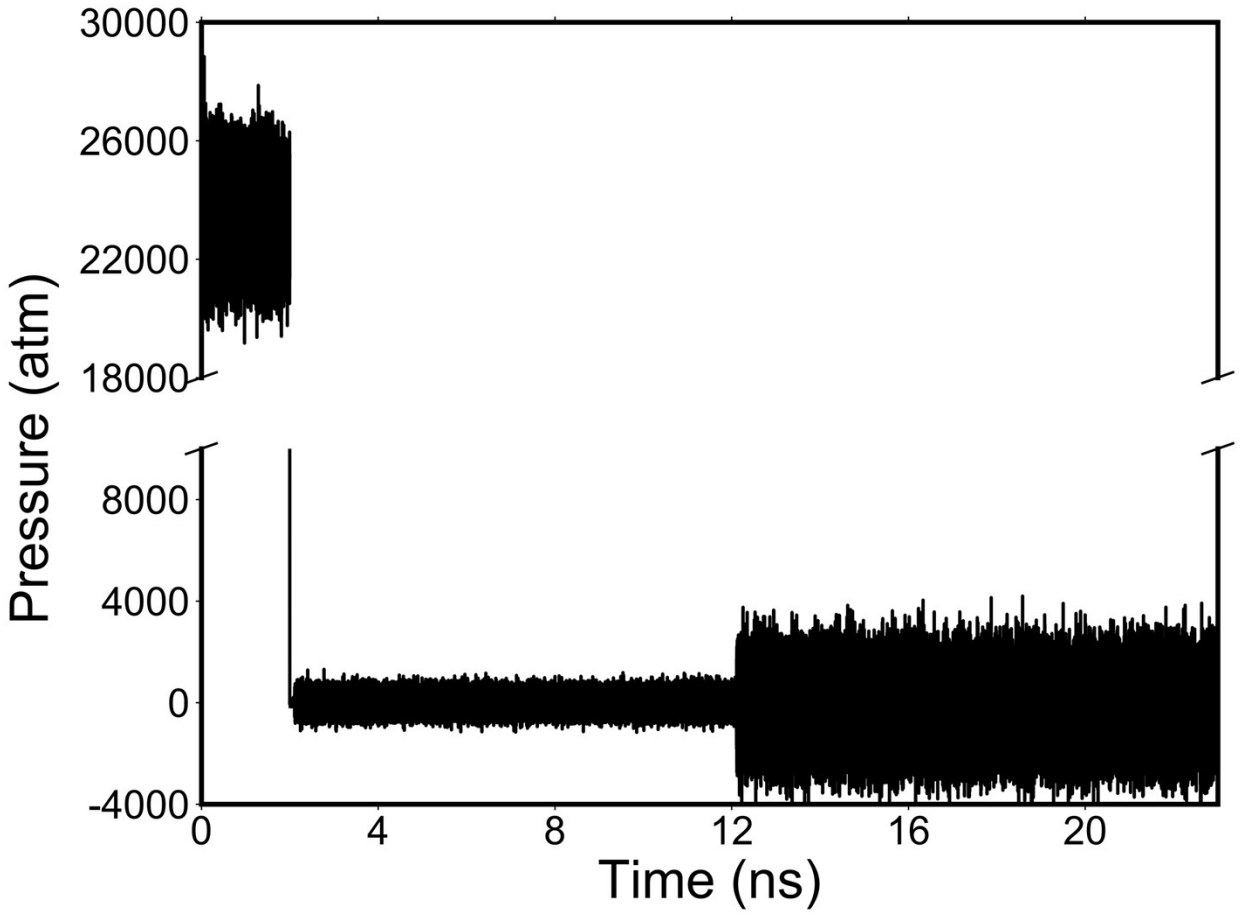

Figure S1. Time evolution of the simulation pressure for bulk pyrophyllite while including the angle bending term. The pressure after the initial 2 ns was noted to be very high (> 23000 atm) and was subsequently equilibrated to 1 atm using the Berendsen thermostat/barostat with small timesteps (see ESI text for full simulation description).

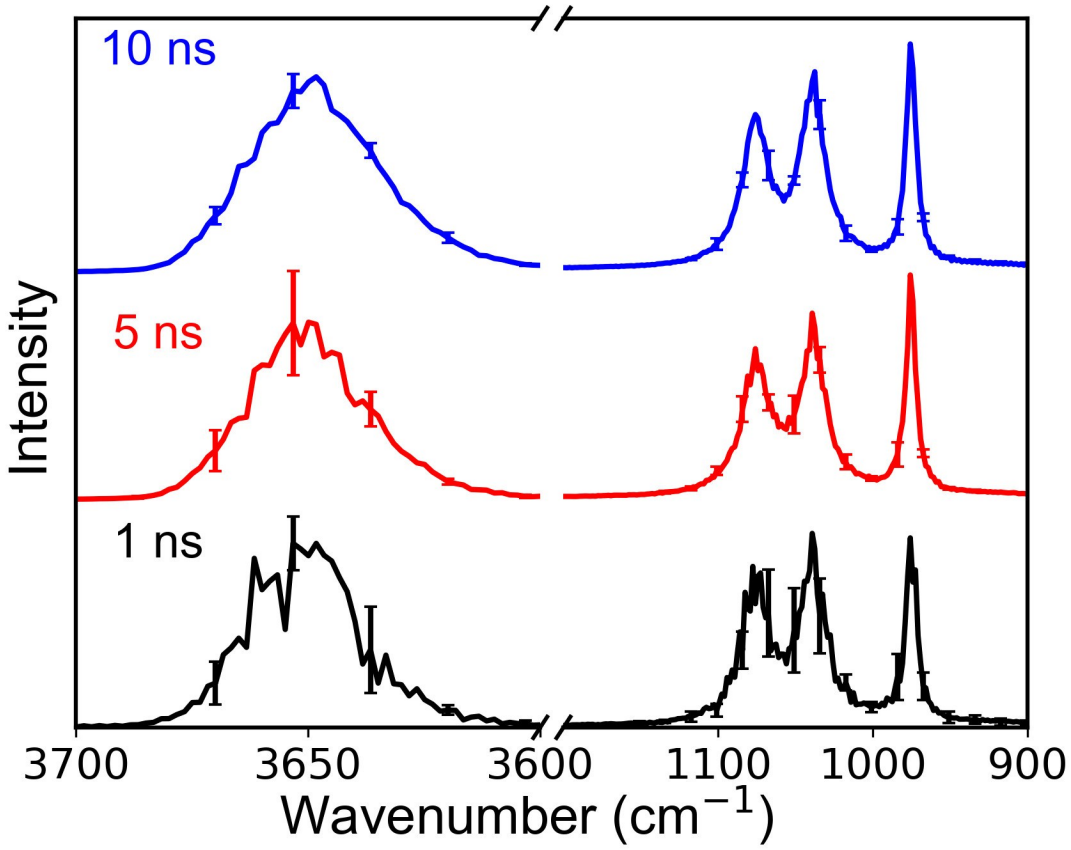

Figure S2. Calculated infrared spectra for bulk pyrophyllite run in the NVE ensemble for 1 ns (black), 5 ns (red), and 10 ns (blue). Simulations were separated into 5 blocks for error bar determinations and a 2 fs delay between new time zeroes in the TCF calculation was used in each case. The intensity in the stretching region of the spectra is ~10% that of the bending region and thus has been amplified for visual clarity.

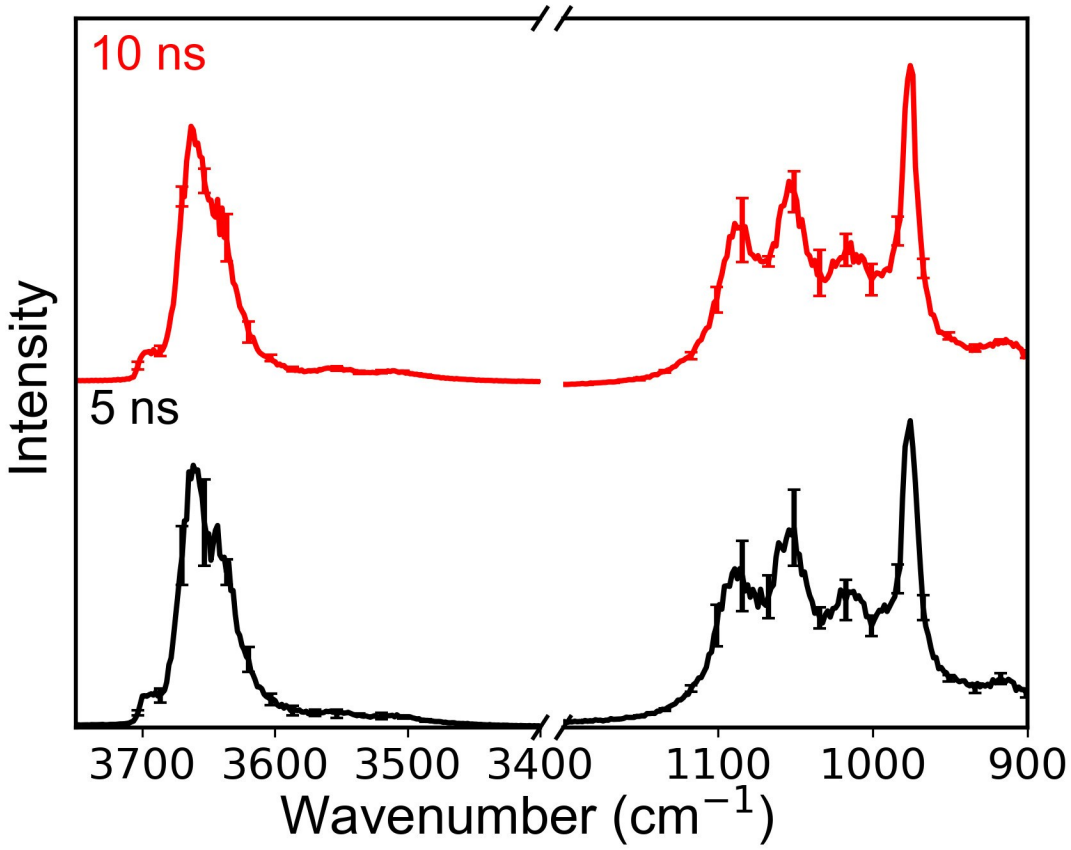

Figure S3. Calculated infrared spectra for the protonated 110 face of pyrophyllite run in the NVE ensemble for 5 ns (black), and 10 ns (red). Simulations were separated into 5 blocks for error bar determinations and a 2 fs delay between new time zeroes in the TCF calculation was used in each case. The intensity in the stretching region of the spectra is ~10% that of the bending region and thus has been amplified for visual clarity.

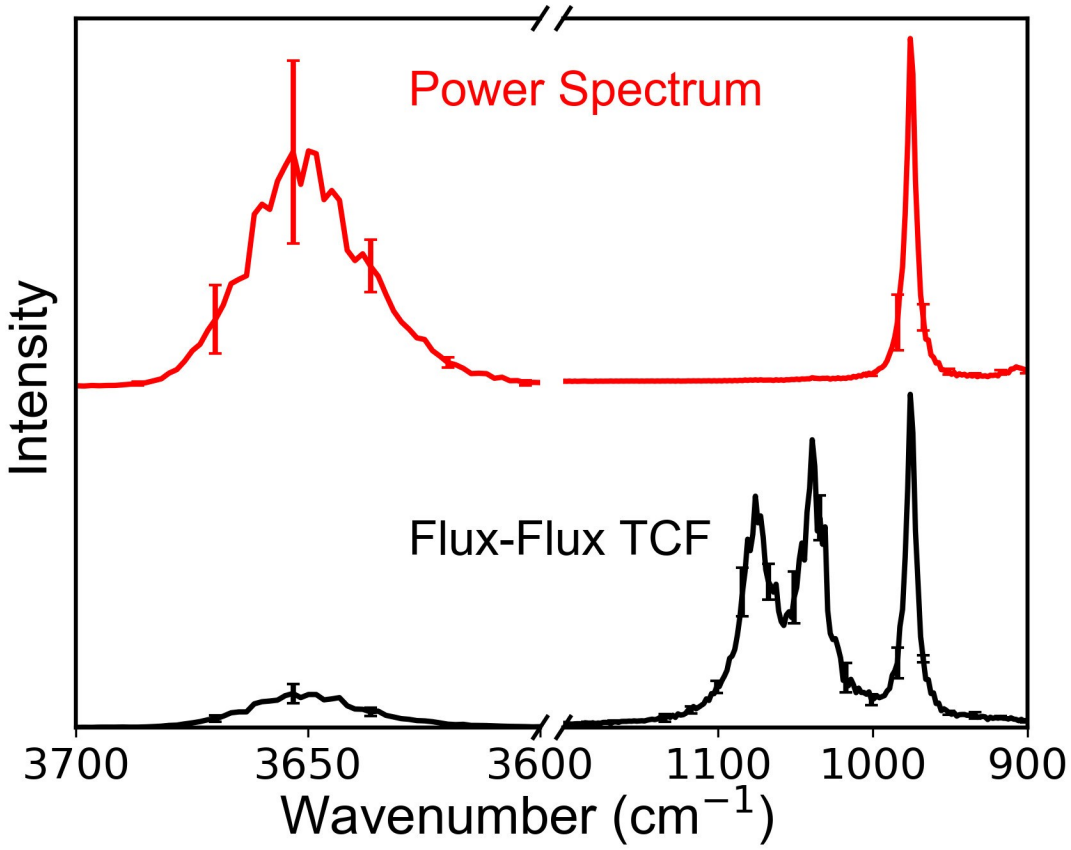

Figure S4. Calculated infrared spectrum for bulk pyrophyllite calculated via the Fourier transform of the velocity autocorrelation function (power spectrum, red) and the electrical flux-flux time correlation function (black). The intensity in the stretching region of the spectra is ~10% that of the bending region and thus has been amplified for visual clarity.

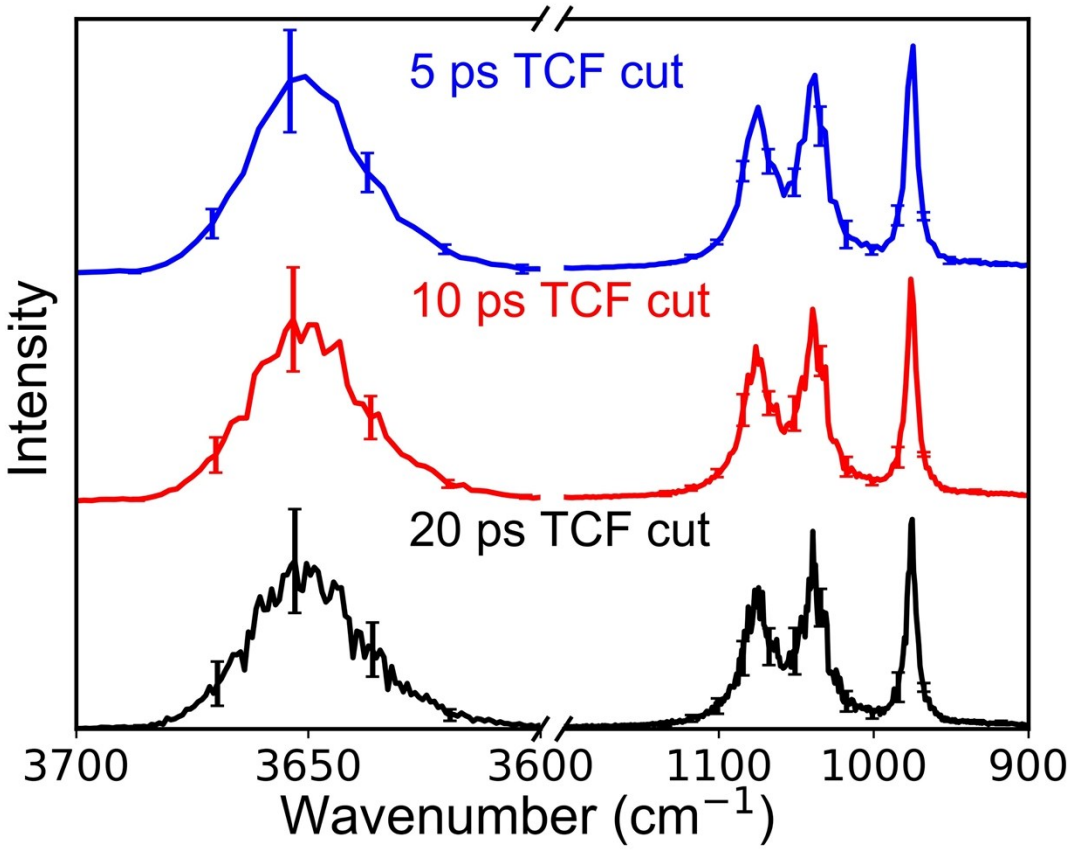

Figure S5. Calculated IR spectrum for bulk pyrophyllite after truncating the TCF at 20 ps (black), 10 ps (red), and 5 ps (blue). Increased length in the TCF increases the noise in the spectrum, while decreased length in the TCF reduces the resolution.

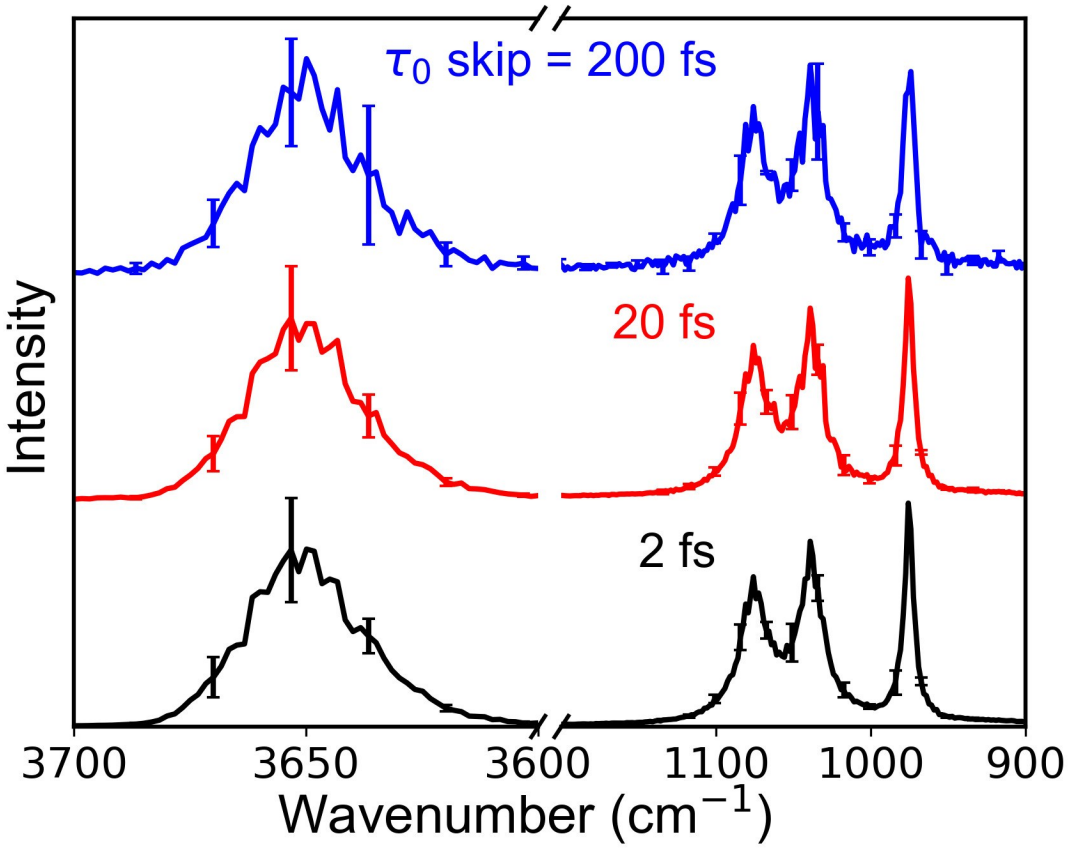

Figure S6. Calculated infrared spectra for bulk pyrophyllite run in the NVE ensemble for 5 ns with a 2 fs (black), 20 fs (red), and 200 fs (blue) time zero delay in the TCF calculation. Simulations were separated into 5 blocks for error bar determinations. The intensity in the stretching region of the spectra is ~10% that of the bending region and thus has been amplified for visual clarity.

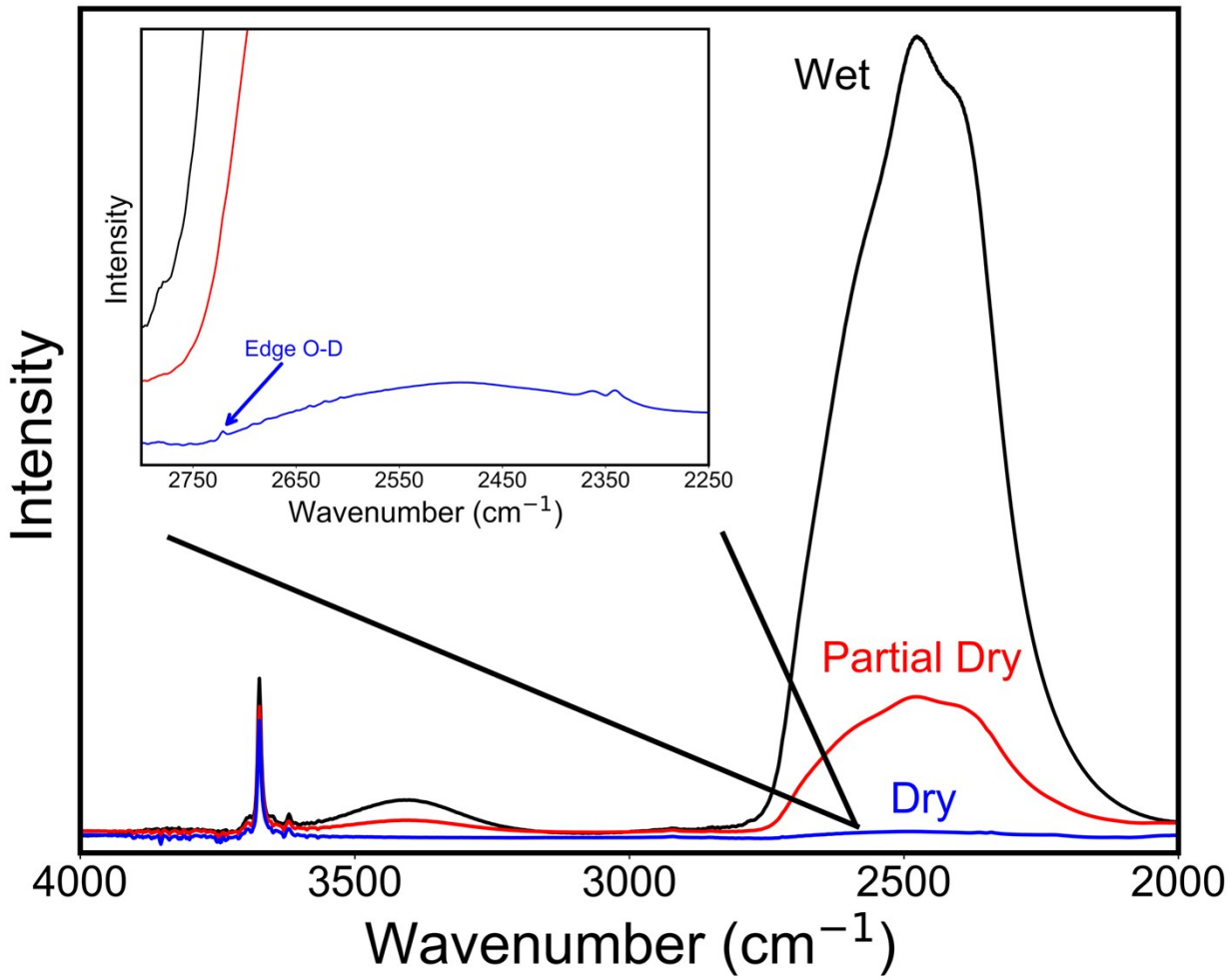

Figure S7. Experimental IR spectra in the stretching region for pyrophyllite in the wet (black), partially dry (red), and final dry (blue) state (also shown in Fig. 3 in the main text). Drying is observed by a decrease in the bulk H_2O (3400 cm^{-1}) and D_2O (2500 cm^{-1}) bands.

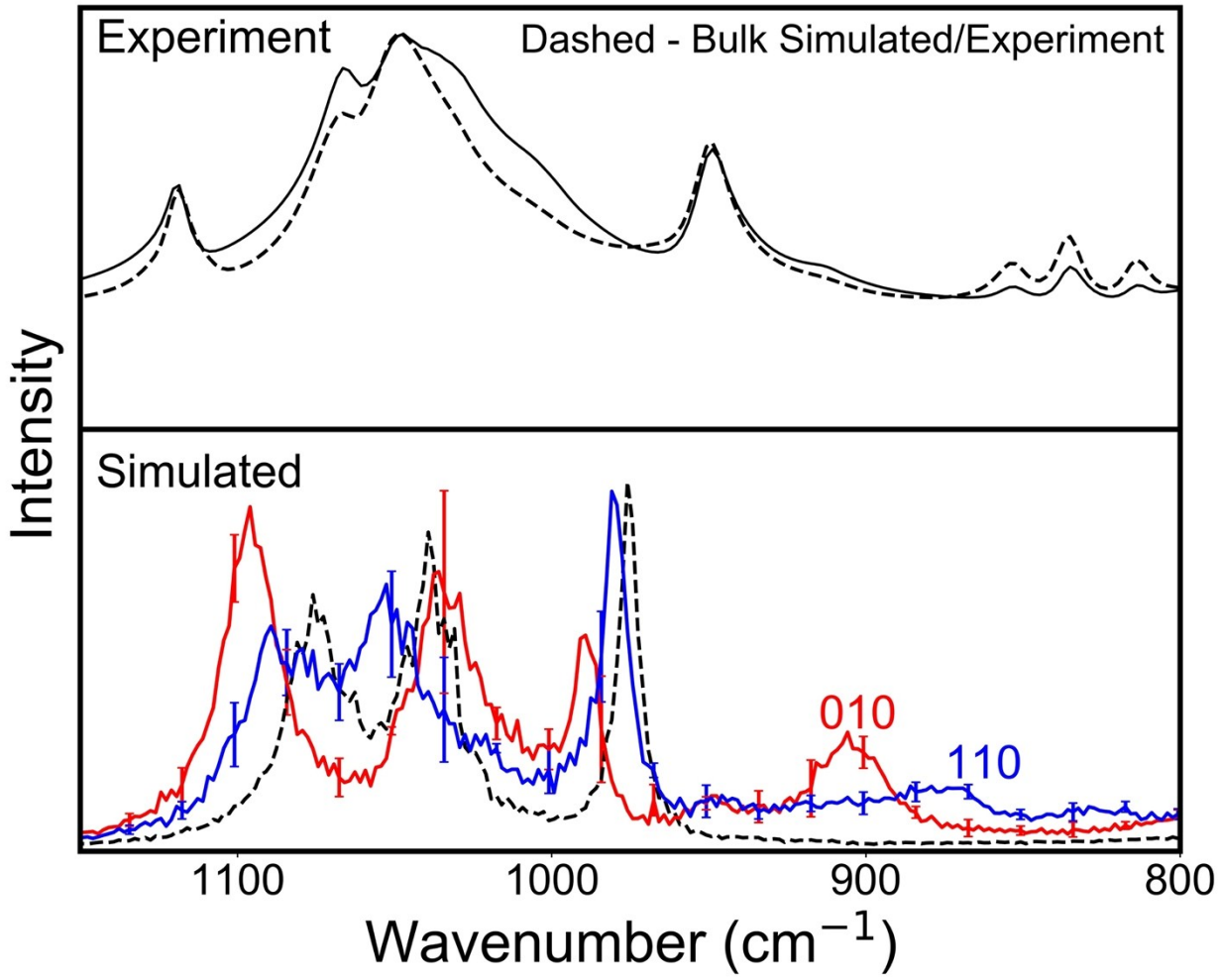

Figure S8. Bending region of the experimental (top) and simulated (bottom) spectra for deuterated edge samples (solid lines) and bulk samples (dashed lines). Simulated spectra are shown for the 010 (red) and 110 (blue) faces. Error bars for the simulated bulk pyrophyllite spectrum are omitted for visual clarity.

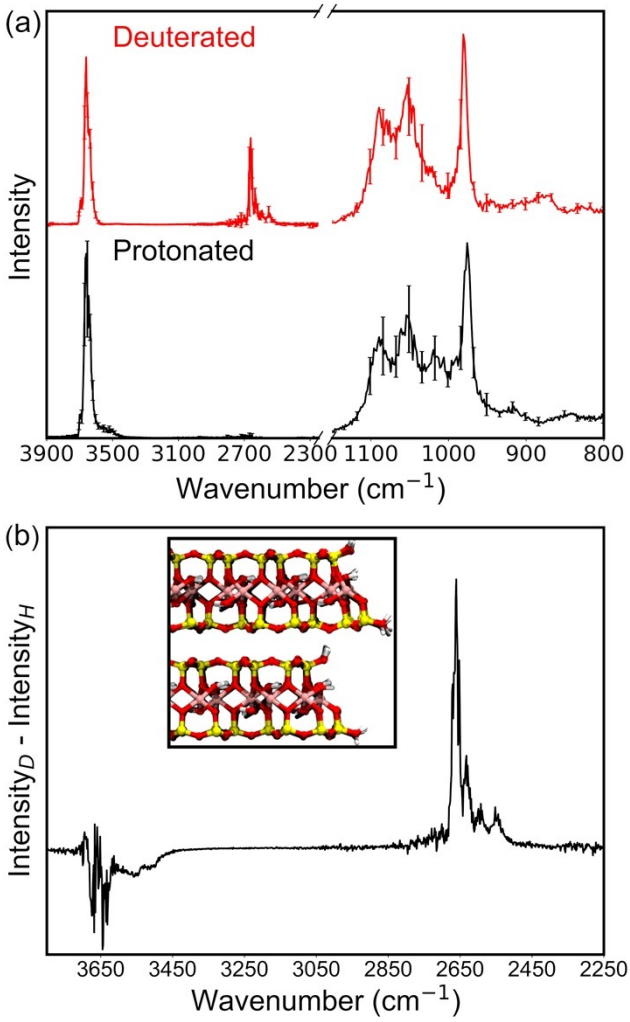

Figure S9. (a) Full infrared spectrum of the protonated (black) and deuterated (red) 110 pyrophyllite edge and (b) difference spectrum between deuterated and protonated spectra for the stretching region. In this spectrum negative peaks represent those that were shifted due to deuteration and positive peaks represent their new positions.

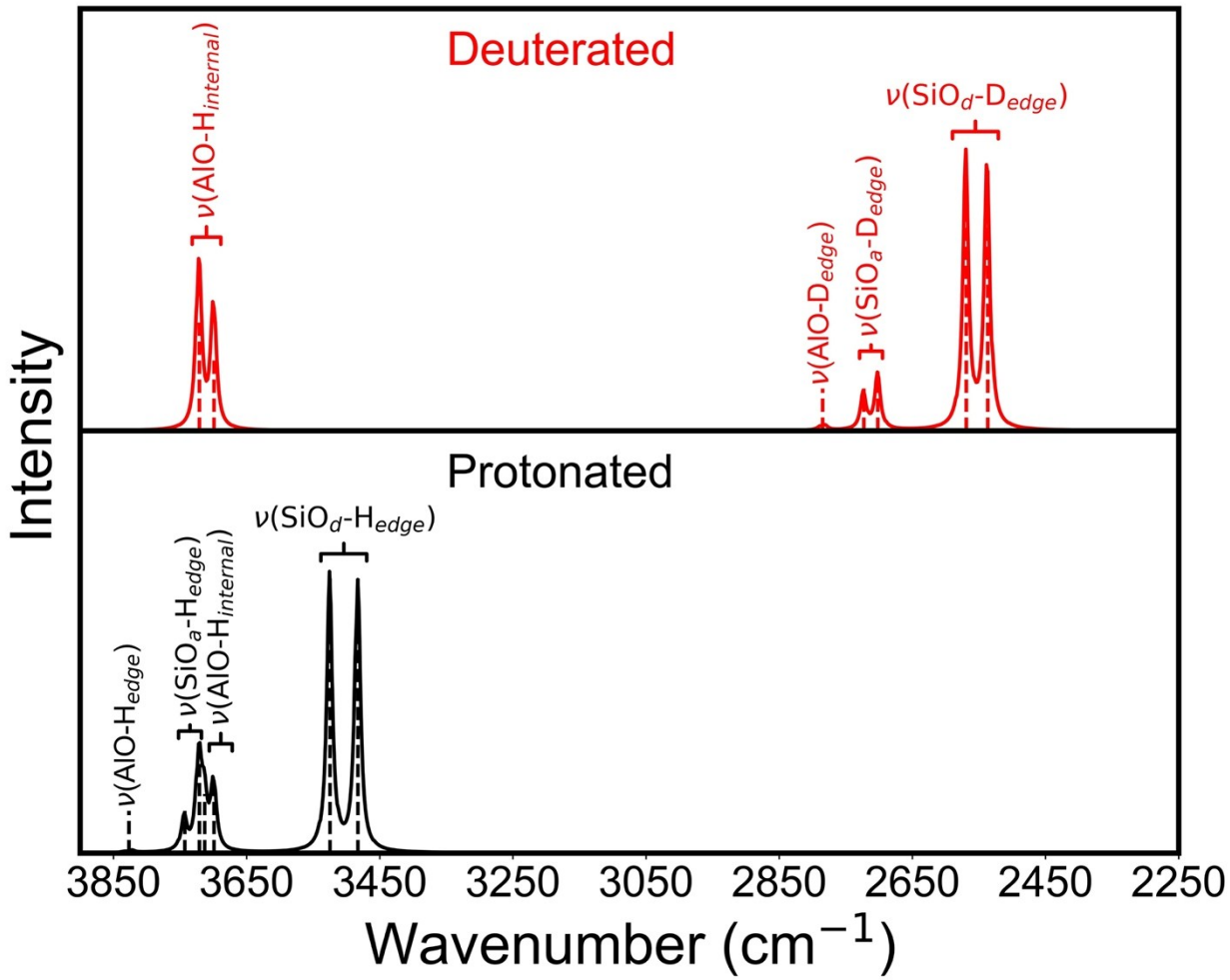

Figure S10. DFT calculated IR spectra for the deuterated (top, red) and protonated (bottom, black) 010 pyrophyllite edge. Relevant modes are indicated which were determined by viewing the modes in J-ICE.[11]

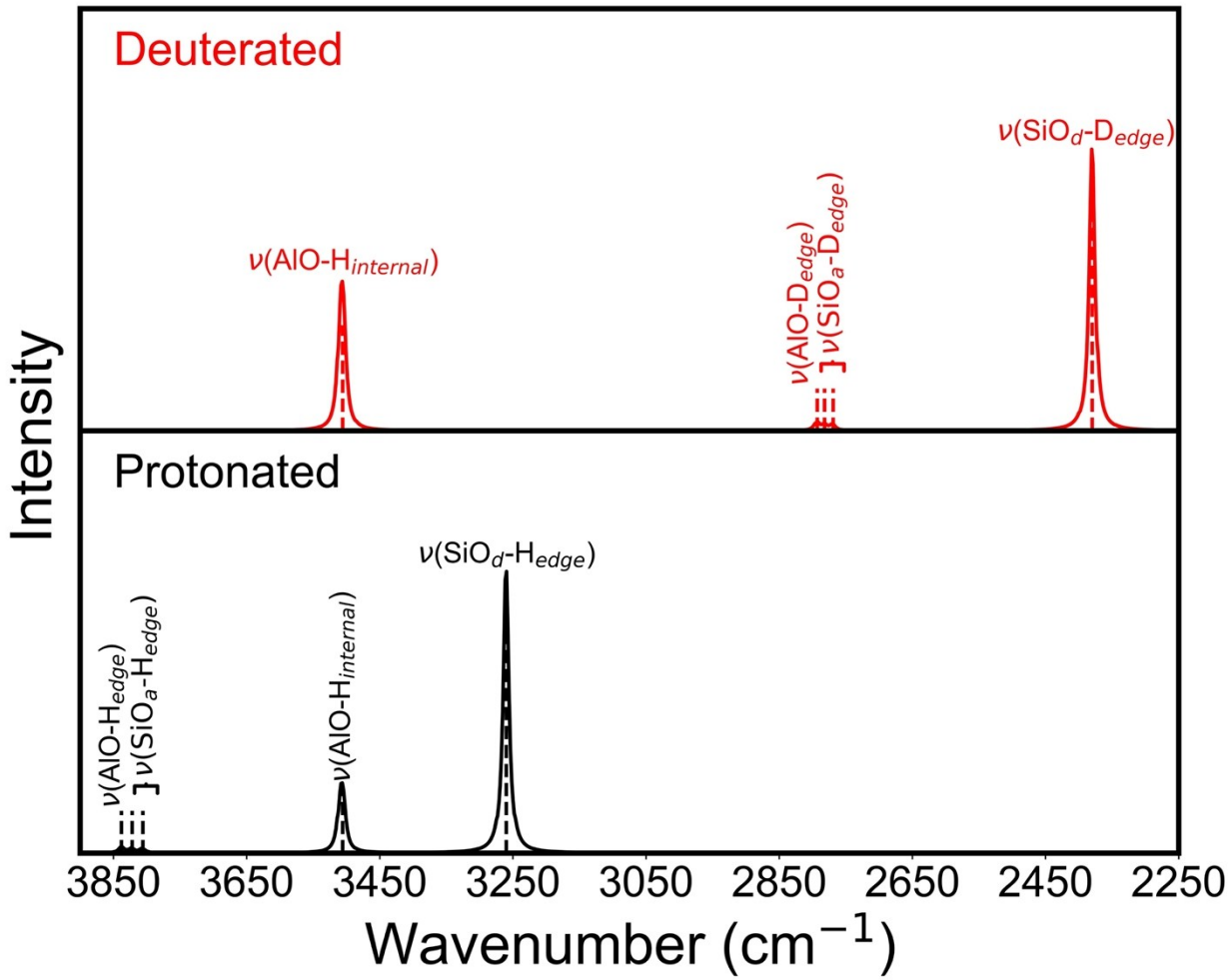

Figure S11. DFT calculated IR spectra for the deuterated (top, red) and protonated (bottom, black) 110 pyrophyllite edge. Relevant modes are indicated which were determined by viewing the modes in J-ICE.[11]

3. References

1. V. A. Drits, S. Guggenheim, B. B. Zviagina and T. Kogure, *Clays and Clay Miner.*, 2012, **60**, 574-587.
2. A. Kremleva, B. Martorell, S. Kruger and N. Rosch, *Phys. Chem. Chem. Phys.*, 2012, **14**, 5815-5823.
3. L. P. Lavikainen, J. T. Hirvi, S. Kasa, T. Schatz and T. A. Pakkanen, *Theor Chem Acc*, 2015, **134**.
4. (a) P. E. Blöchl, *Phys. Rev. B*, 1994, **50**, 17953-17979; (b) G. Kresse and D. Joubert, *Phys. Rev. B*, 1999, **59**, 1758-1775.
5. (a) G. Kresse and J. Hafner, *Phys. Rev. B*, 1993, **47**, 558-561; (b) G. Kresse and J. Hafner, *Phys. Rev. B*, 1994, **49**, 14251-14269; (c) G. Kresse and J. Furthmuller, *Comp. Mater. Sci.*, 1996, **6**, 15-50; (d) G. Kresse and J. Furthmuller, *Phys. Rev. B*, 1996, **54**, 11169-11186.
6. J. P. Perdew, A. Ruzsinszky, G. I. Csonka, O. A. Vydrov, G. E. Scuseria, L. A. Constantin, X. Zhou and K. Burke, *Phys. Rev. Lett.*, 2008, **100**, 136406.
7. (a) S. Grimme, J. Antony, S. Ehrlich and H. Krieg, *J. Chem. Phys.*, 2010, **132**, 154104; (b) S. Grimme, S. Ehrlich and L. Goerigk, *J. Comput. Chem.*, 2011, **32**, 1456-1465.
8. J. H. Lee and S. Guggenheim, *Am. Miner.*, 1981, **66**, 350-357.
9. S. V. Churakov, *J. Phys. Chem. B*, 2006, **110**, 4135-4146.
10. (a) P. Giannozzi, S. de Gironcoli, P. Pavone and S. Baroni, *Phys. Rev. B*, 1991, **43**, 7231-7242; (b) P. Giannozzi and S. Baroni, *J. Chem. Phys.*, 1994, **100**, 8537-8539; (c) S. Baroni, S. de Gironcoli, A. Dal Corso and P. Giannozzi, *Rev Mod Phys*, 2001, **73**, 515-562; (d) D. Karhanek, T. Bucko and J. Hafner, *J. Phys. Condens. Matter.*, 2010, **22**, 265006.
11. P. Canepa, R. M. Hanson, P. Ugliengo and M. Alfredsson, *J Appl Crystallogr*, 2011, **44**, 225-229.
12. S. Plimpton, *J. Comput. Phys.*, 1995, **117**, 1-19.
13. R. T. Cygan, J.-J. Liang and A. G. Kalinichev, *The Journal of Physical Chemistry B*, 2004, **108**, 1255-1266.
14. M. Pouvreau, J. A. Greathouse, R. T. Cygan and A. G. Kalinichev, *J. Phys. Chem. C*, 2017, **121**, 14757-14771.
15. P. P. Ewald, *Annalen der Physik*, 1921, **369**, 253-287.
16. M. Tuckerman, B. J. Berne and G. J. Martyna, *J. Chem. Phys.*, 1992, **97**, 1990-2001.
17. H. J. C. Berendsen, J. P. M. Postma, W. F. van Gunsteren, A. DiNola and J. R. Haak, *J. Chem. Phys.*, 1984, **81**, 3684-3690.
18. C. W. Garland, J. W. Nibler and D. P. Shoemaker, *Experiments in Physical Chemistry*, McGraw-Hill Higher Education, 2009.
19. D. A. McQuarrie, *Statistical mechanics / Donald A. McQuarrie*, Harper & Row, New York, 1975.
20. (a) P. Bornhauser and D. Bougeard, *J. Phys. Chem. B*, 2001, **105**, 36-41; (b) B. Boulard, J. Kieffer, C. C. Phifer and C. A. Angell, *J Non-Cryst Solids*, 1992, **140**, 350-358; (c) M. Praprotnik and D. Janezic, *J. Chem. Phys.*, 2005, **122**, 174103; (d) V. Agarwal, G. W. Huber, W. C. Conner, Jr. and S. M. Auerbach, *J. Chem. Phys.*, 2011, **135**, 134506.

21. J. A. Greathouse, J. S. Durkin, J. P. Larentzos and R. T. Cygan, *J. Chem. Phys.*, 2009, **130**, 134713.
22. American Petroleum Institute, *Clay mineral standards; American Petroleum Institute [research] project 49. Preliminary report no. 1-8.*, New York, 1950.